PHYSICAL REVIEW B VOLUME 56, NUMBER 20 15 NOVEMBER 1997-II

Surface electronic structure with the linear methods of band theory

E. E. Krasovskii* and W. Schattke
Institut für Theoretische Physik, Christian-Albrechts-Universität, Leibnizstrasse 15, D-24118 Kiel, Federal Republic of Germany

(Received 27 November 1996; revised manuscript received 2 June 1997)

We present an *ab initio* method for calculating electron states in a semi-infinite crystal. The complex band structure is obtained by the extended linear augmented-plane-wave method within the exact $\mathbf{k}\cdot\mathbf{p}$ formulation of the band-structure problem. We also present a variational scheme of matching the wave functions at the interface. The practical applicability of the method is demonstrated by solving the Schrödinger equation for the (100) surface of Al. We have calculated the normal incidence low-energy electron-diffraction spectra, the occupied surface state at the Γ point, and the normal-emission photoelectron spectra within the one-step model. The results are in a good agreement with available measurements. We have developed a simplified procedure to assess the conducting properties of a crystal surface in terms of the $\boldsymbol{k}_{\parallel}$-projected real band structure. We introduce a new quantity, the conductance index, whose energy dependence is shown to yield gross features of the exact energy dependence of transmitted current. [S0163-1829(97)05343-5]

I. INTRODUCTION

Photoemission measurements carry rich information about the electronic structure of the crystal. To extract the characteristics of the electronic structure theoretical models are invoked, which are not, in general, free from adjustable parameters. The unambiguous interpretation of the spectra requires minimization of the number of such parameters, which is achieved by applying first-principles computational methods.

The *ab initio* treatment of the electronic structure of the semi-infinite crystal is based on the numerical solution of the Schrödinger equation, with the domain composed of the bulk and vacuum half spaces. The mathematical formulation of the problem depends upon which method is employed to obtain the function satisfying the Schrödinger equation in the bulk half space. One of the earliest approaches, the propagation matrix technique of Marcus and Jepsen,[1] leads to a system of differential equations, which is solved by step-by-step integration. Present day calculations are based either on the Bloch wave approach[2] or on the multiple-scattering technique.[3] In the Bloch wave method one takes advantage of the fact that far from the crystal surface the solution is a linear combination of the wave functions that satisfy the bulk Schrödinger equation, thereby taking into account all multiple scattering in the crystal.[2] This linear combination is matched at a plane parallel to the surface to the solutions in the surface region.[4] The multiple-scattering technique is based on the layer Korringa-Kohn-Rostoker (KKR) method.[5] In this method the crystal is represented as a finite number of monolayers and the convergence is ensured by introducing the electron absorption as an imaginary part of the crystal potential. The layer KKR method employs the angular-momentum representation of the solution in the solid, which makes the method very efficient for potentials of the muffin-tin form.[3] Recently, the layer KKR method has been extended to the case of the space-filling potentials of arbitrary shape[6] by employing the phase functional ansatz.

It should be noted that even in the case of three-dimensional translational invariance it is not trivial to get a solution accurate everywhere in the unit cell.[7] The photoelectron final states are strongly delocalized: Even for the close-packed crystal structures the probability of finding the electron outside the muffin-tin sphere exceeds 30%; therefore, to get an accurate wave function far from the nucleus one has to retain a large number of terms in the angular-momentum expansion of the scattering theory. For open structures with several molecules per unit cell the KKR approach would lead to very time-consuming calculations.

The recent progress in the linear methods of band theory suggests a way to avoid these difficulties.[7] It has been shown that using an extended radial basis set in the exact $\mathbf{k}\cdot\mathbf{p}$ formulation of the Schrödinger equation makes it possible to solve the band-structure problem for real and complex Bloch vectors with any desired accuracy.[8] This offers a possibility to apply the efficient linear band-structure methods to the semi-infinite crystal problem in the framework of the Bloch wave approach.

Until now this approach has been used only in pseudopotential calculations; in the present work we extend its application to the case of a singular crystal potential by using the extended linear augmented-plane-wave (ELAPW) $\mathbf{k}\cdot\mathbf{p}$ method. This enables us to obtain accurate wave functions and opens a way to employ the elaborate full-potential linear augmented-plane-wave (LAPW) technique[9] in photoemission and also in low-energy electron-diffraction (LEED) calculations. The method we propose is expected to be advantageous for very low energies, where the scattering by the singular potential is strong and the electron absorption is small.

In Sec. II we describe the formalism of the direct and inverse ELAPW $\mathbf{k}\cdot\mathbf{p}$ methods and discuss its accuracy. In Sec. III we present a method of matching the functions at the crystal surface and propose a fast procedure to estimate the conducting properties of the surface. In Sec. IV the inverse ELAPW is applied to the calculation of the localized surface state at the (100) surface of aluminum. The possible errors due to our neglect of the quasiparticle effects are discussed in Sec. V. In Sec. VI the (100) normal emission photoelectron spectra of Al are compared with the experiment.

II. ELAPW k·p METHOD

A. Formalism

In the ELAPW method the trial function with the Bloch vector $\boldsymbol{k}_0$ is a linear combination of $N_{\boldsymbol{G}}$ energy-independent augmented plane waves[10] (APW's)

$$\Psi_i(\boldsymbol{k}_0,\boldsymbol{r})=\sum_{l,m} 4\pi i^l u_l(K_i,r)Y^*_{lm}(\hat{\boldsymbol{K}}_i)Y_{lm}(\hat{\boldsymbol{r}}),$$

$$\boldsymbol{K}_i=\boldsymbol{k}_0+\boldsymbol{G}_i, \tag{1}$$

$\boldsymbol{G}_i$ being reciprocal lattice vectors and $N-N_{\boldsymbol{G}}$ localized functions[8]

$$Z_{nlm}(\boldsymbol{r})=z_{nl}(r)Y_{lm}(\hat{\boldsymbol{r}}),\quad n=1,\ldots,N_l,$$

$$N-N_{\boldsymbol{G}}=\sum_{l=0}^{l_{\max}} N_l(2l+1), \tag{2}$$

the additional Z functions being referred to as the extension of the LAPW basis set. The radial function $u_l(K_i,r)$ is a linear combination of the solution $\phi_{\nu l}$ of the radial Schrödinger equation at energy $E_{\nu l}$ and its energy derivative $\dot{\phi}_{\nu l}$, which matches the Bessel function $j_l(K_i r)$ in both value and slope at the muffin-tin sphere boundary.

In the ELAPW we choose $N_l=2$ for all $l\leqslant l_{\max}$, so the dimension of the Hamiltonian matrix is

$$N=N_{\boldsymbol{G}}+2(l_{\max}+1)^2.$$

To construct the localized function we choose an additional energy parameter $E_{\mu l}$ so that z_{nl} ($n=1,2$) are two linear combinations of four functions $\phi_{\nu l}$, $\dot{\phi}_{\nu l}$, $\phi_{\mu l}$, and $\dot{\phi}_{\mu l}$, which have both zero value and zero slope at the sphere radius and vanish in the interstitial.

In the **k·p** method we choose a reference point $\boldsymbol{k}_0$ and represent the wave function with the Bloch vector $\boldsymbol{k}$ and the band index λ as a product of the phase factor $\exp[i(\boldsymbol{k}-\boldsymbol{k}_0)\boldsymbol{r}]$ and the trial function having the Bloch vector $\boldsymbol{k}_0$, $\Psi_{\boldsymbol{k}_0}$:

$$\Psi(\boldsymbol{k},\lambda,\boldsymbol{r})=\exp(i\Delta\boldsymbol{k}\cdot\boldsymbol{r})\Psi_{\boldsymbol{k}_0}(\boldsymbol{k},\lambda,\boldsymbol{r}),$$

$$\Delta\boldsymbol{k}=\boldsymbol{k}-\boldsymbol{k}_0,$$

$$\Psi_{\boldsymbol{k}_0}(\boldsymbol{k},\lambda,\boldsymbol{r})=\sum_{i=1}^{N} C_i(\boldsymbol{k},\lambda)\psi_i(\boldsymbol{k}_0,\boldsymbol{r}). \tag{3}$$

The localized functions do not depend on $\boldsymbol{k}_0$, but we use the same notation for all the basis functions for the sake of brevity.[11]

Then the Schrödinger equation

$$\hat{H}\Psi(\boldsymbol{k},\lambda)=E\Psi(\boldsymbol{k},\lambda) \tag{4}$$

leads to the matrix equation

$$[\hat{H}_{\boldsymbol{k}_0}+2\Delta\boldsymbol{k}\cdot\hat{\boldsymbol{P}}_{\boldsymbol{k}_0}+(\Delta k^2-E)\hat{O}_{\boldsymbol{k}_0}]\boldsymbol{C}_{\boldsymbol{k}\lambda}=0,$$

$$H_{ij}=\langle\psi_i(\boldsymbol{k}_0)|-\Delta+V(\boldsymbol{r})|\psi_j(\boldsymbol{k}_0)\rangle,$$

$$O_{ij}=\langle\psi_i(\boldsymbol{k}_0)|\psi_j(\boldsymbol{k}_0)\rangle,$$

$$\boldsymbol{P}_{ij}=\langle\psi_i(\boldsymbol{k}_0)|-i\boldsymbol{\nabla}|\psi_j(\boldsymbol{k}_0)\rangle. \tag{5}$$

In the direct **k·p** we fix the target point $\boldsymbol{k}$ and solve the eigenvalue problem for the energies E. Real $\boldsymbol{k}$ vectors yield the real band structure and real eigenvalues corresponding to complex $\boldsymbol{k}$ vectors comprise the complex band structure.

B. Accuracy

The high accuracy of the ELAPW **k·p** method is due to the additional radial functions used to construct the lmth orbital χ_{lm} in the angular-momentum expansion of the function $\Psi_{\boldsymbol{k}_0}$. In practical calculations the distance to the target point is not too large, $\Delta k<2\pi/a$; therefore, the term $l=0$ dominates in the Rayleigh decomposition of the plane wave $\exp(i\Delta\boldsymbol{k}\cdot\boldsymbol{r})$. In the usual ELAPW the flexibility of the basis set[7] is used to adjust the function χ_{lm} to the solution of the radial Schrödinger equation ϕ_l, whereas the task of the ELAPW **k·p** method is to fit the orbital χ_{lm} to the exact solution ϕ_l divided by the leading Bessel function

$$\phi_l(E_{\boldsymbol{k}\lambda},r)/j_0(\Delta kr).$$

The error of this fit is rather small because χ_{lm} still has variational freedom after the conditions of matching to the interstitial have been satisfied. However, to get a precise solution for an electron state having a considerable contribution of angular momentum l_0 one has to include additional functions with $l=l_0\pm1$ because the matrix equation (5) involves large momentum matrix elements $\langle l_0\pm1|-i\boldsymbol{\nabla}|l_0\rangle$.

We have examined the accuracy of the ELAPW **k·p** scheme in Ref. 8, having chosen copper as an example. Here we briefly recall the main results of this study. The reference point was chosen at the center of gravity of the irreducible part of the Brillouin zone and the energies $E_{\boldsymbol{k}\lambda}$ were calculated on a uniform $\boldsymbol{k}$-point mesh by the ELAPW **k·p** method and by the pure ELAPW. The reference-target-distance range covered by the $\Delta\boldsymbol{k}$ vectors is shown in Fig. 1: The Δk dependence of the error is averaged over the directions of $\Delta\boldsymbol{k}$ and over the energy interval from the bottom of the valence band to 0.5 Ry above the Fermi level. Four basis sets have been considered containing Z functions of angular momenta up to $l_{\max}$=1, 2, 3, and 5.

It is seen that the energy error is a power function of the distance from the reference point. The largest errors occur for the highly localized d states, where the shape of the wave function inside the sphere affects the energy strongly. In accord with the above argumentation, the accuracy is not improved by adding the functions of d character, but including the f functions reduces the error by an order of magnitude. The further extension of the radial basis set, up to $l_{\max}$=5, has no effect on the performance of the method. For the free-electron-like states, where the orbitals χ_{lm} are closer to Bessel functions, the errors are not expected to be larger than in the considered case.

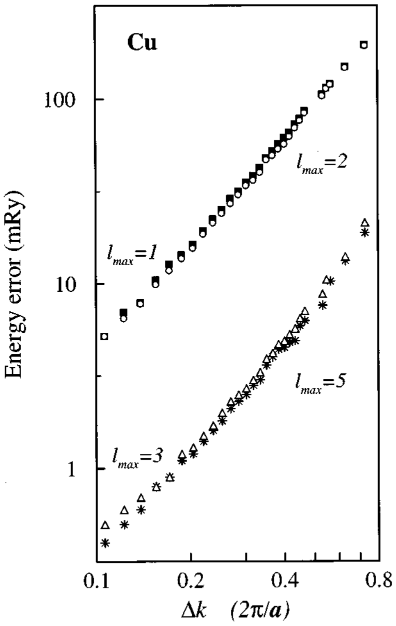

FIG. 1. Energy error of the ELAPW **k·p** method vs the distance from the reference point for several extensions: $l_{\max}=1$ (squares), 2 (circles), 3 (triangles), and 5 (stars).

C. Inverse ELAPW k·p

In the present work we use the ELAPW **k·p** method to solve the inverse band-structure problem; i.e., given two real Cartesian components of the Bloch vector $\boldsymbol{k}_{\parallel}=(k_x,k_y)$ and the energy E, we find the values of $k_{\perp}$ that satisfy the Schrödinger equation

$$\hat{H}\Psi_n(E,\boldsymbol{k}_{\parallel},k_{\perp n};\boldsymbol{r})=E\Psi_n(E,\boldsymbol{k}_{\parallel},k_{\perp n};\boldsymbol{r}), \tag{6}$$

with the complex Bloch vector $\boldsymbol{k}=(\boldsymbol{k}_{\parallel},k_{\perp})$. The choice of reference point depends upon $\boldsymbol{k}_{\parallel}$: $\boldsymbol{k}_0=(\boldsymbol{k}_{\parallel},k_{\perp 0})$. $k_{\perp 0}$ is arbitrary, usually it is chosen at the center of the $k_{\perp}$ interval of interest. Now the **k·p** representation

$$\Psi_n(\boldsymbol{\rho},z)=\exp(i\Delta k_{\perp n}z)\sum_i C_{in}(E,\boldsymbol{k}_0)\,\psi_i(\boldsymbol{k}_0,\boldsymbol{r}),$$

$$k_{\perp n}=k_{\perp 0}+\Delta k_{\perp n},$$

$$\boldsymbol{\rho}=(\rho_x,\rho_y), \tag{7}$$

leads to the matrix equation

$$[\hat{H}+2\Delta k_{\perp n}\hat{P}_{\perp}+(\Delta k_{\perp n}^2-E)\hat{O}]\boldsymbol{C}_n=0,$$

$$\hat{P}_{\perp}=\hat{\boldsymbol{P}}\cdot\boldsymbol{n}_z. \tag{8}$$

We define the vector $\boldsymbol{D}_n=-(2\hat{P}_{\perp}+\Delta k_{\perp n}\hat{O})\boldsymbol{C}_n$ and reduce Eq. (8) to a matrix equation of twice the dimension:

$$\begin{pmatrix} 0 & \hat{H}-E\hat{O} \\ \hat{I} & 2\hat{P}_{\perp} \end{pmatrix}\begin{pmatrix} \boldsymbol{D}_n \\ \boldsymbol{C}_n \end{pmatrix}=\Delta k_{\perp n}\begin{pmatrix} \hat{I} & 0 \\ 0 & -\hat{O} \end{pmatrix}\begin{pmatrix} \boldsymbol{D}_n \\ \boldsymbol{C}_n \end{pmatrix}. \tag{9}$$

Thus the solutions of the inverse band-structure problem $\Delta k_{\perp n}$ are obtained as solutions of the generalized non-Hermitian eigenvalue problem.

Solutions of Eq. (6) are orthogonal in the sense that at the plane $z=\text{const}$ the nondiagonal elements of the current operator vanish:

$$\int_S\left[\left(-i\frac{d}{dz}\Psi_n\right)\Psi_{n'}^{*}-\left(-i\frac{d}{dz}\Psi_{n'}^{*}\right)\Psi_n\right]d\boldsymbol{\rho}=0. \tag{10}$$

Here the integral is over the surface of the unit cell. In other words, the current carried by a sum of the Bloch states with the same E and $\boldsymbol{k}_{\parallel}$ is the sum of the individual currents.[1]

Consider an evanescent wave with the Bloch vector $k_{\perp}=k_{\perp 1}+ik_{\perp 2}$. From Eq. (8) it follows that for the Bloch part of the wave function $\Psi_{\boldsymbol{k}_{\parallel},k_{\perp 1}}$ [see Eq. (3)] the expectation value of the momentum operator $\hat{P}_{\perp}$ vanishes and its energy expectation value is equal to $k_{\perp 2}^2+E$. It is well known that the higher the energy of the Bloch state, the poorer its convergence, i.e., the larger the number of plane waves (or, equivalently, the number of spherical functions) that must be included in the basis set. This means that the accuracy of the evanescent waves deteriorates with increasing the imaginary part of the Bloch vector irrespective of the method of calculation.

Evidently, the above formalism is not restricted to the APW-like methods. For a linear method to be applied within the exact **k·p** formulation it is only required that the extended radial basis set be used in constructing the trial function. Recently, an extended formalism has been developed for the linear muffin-tin orbital (LMTO) method[12] (multiple orbitals per lm channel) and the usual limitations of the rigid linear methods (see Ref. 7) have been eliminated. As in the usual band-structure calculations, solving the inverse problem with the LMTO method may be preferable in the cases when the atomic sphere approximation is plausible, as the LMTO method is much less time consuming than the ELAPW method.

III. MATCHING THE SOLUTIONS AT THE CRYSTAL SURFACE

Consider the electron wave functions in the semi-infinite crystal. The domain now comprises the bulk half space and vacuum. Let E be an energy at which there exists a solution of the Schrödinger equation in the whole space. In the bulk $(z\leqslant 0)$ far from the crystal surface the solution Φ is a linear combination of the eigenfunctions Ψ_n satisfying Eqs. (6) and (7), with $\mathrm{Im}(k_{\perp n})=0$ for propagating Bloch states and $\mathrm{Im}(k_{\perp n})<0$ for evanescent states.

Consider the case of a Bloch electron incident from the solid. Let Ψ_{λ} be its wave function, i.e., the λth propagating solution of Eq. (9). Then the scattering by the crystal surface is described by the wave function Φ_{λ}, which has the following asymptotics at $z\rightarrow-\infty$:

$$\Phi_{\lambda}(\boldsymbol{\rho},z)=b_0\Psi_{\lambda}(\boldsymbol{\rho},z)+\sum_{n=1}^{N_{sol}} b_n\Psi_n(\boldsymbol{\rho},z), \tag{11}$$

where Ψ_n are reflected Bloch waves, which propagate or decay into the solid.

In a local band gap of the energy spectrum there are no propagating solutions, so $\Psi_{\lambda}=0$. Still there may exist a localized surface state with the wave function decaying both into the vacuum and into the solid.

In the vacuum, where the potential is zero, the solution is a linear combination of plane waves

$$\Phi_\lambda(\boldsymbol{\rho},z)=\sum_s a_s^+\phi_s^+(\boldsymbol{\rho},z), \tag{12}$$

$$\phi_s(\boldsymbol{\rho},z)=\exp[i(\boldsymbol{k}_\parallel+\boldsymbol{G}_s)\boldsymbol{\rho}+ik_sz], \tag{13}$$

$$|\boldsymbol{k}_\parallel+\boldsymbol{G}_s|^2+k_s^2=E, \tag{14}$$

$$\mathrm{Im}(k_s)\geqslant 0,$$

$\boldsymbol{G}_s$ being the surface reciprocal lattice vectors. The superscript $+$ $(-)$ denotes the plane waves propagating or decaying to $z=+$ $(-)$ ∞. In the case of the incident Bloch electron this sum contains the waves propagating or decaying into vacuum and in the case of the surface state it contains only decaying waves.

For LEED states the asymptotics is given in the vacuum, at $z\rightarrow+\infty$; it is defined by fixing the (nonzero) coefficient of the incident plane wave ϕ_0^-. In the vacuum

$$\Phi_{\mathrm{LEED}}(\boldsymbol{\rho},z)=a_0^-\phi_0^-(\boldsymbol{\rho},z)+\sum_s a_s^+\phi_s^+(\boldsymbol{\rho},z) \tag{15}$$

and in the solid it is a sum of the Bloch states that transmit the incident current

$$\Phi_{\mathrm{LEED}}(\boldsymbol{\rho},z)=\sum_{n=1}^{N_{sol}} b_n\Psi_n(\boldsymbol{\rho},z). \tag{16}$$

In a local band gap the LEED wave function describes a totally reflected electron beam.

A. Matching problem

In the case of a steplike surface barrier, with a periodic bulk potential $V(\boldsymbol{r})$ for $z<0$ and a zero potential for $z\geqslant 0$, the two representations in both half spaces hold right to the surface and the coefficients are determined by matching the wave function and its derivative over the plane $z=0$. At a plane $z=\mathrm{const}$ the eigenfunctions $\Psi_n(\boldsymbol{\rho},z)$ are expanded into the two-dimensional Fourier series

$$\Psi_n(\boldsymbol{\rho},z)=\sum_{s=0}^{N_F-1} f_{sn}(z)\exp[i(\boldsymbol{k}_\parallel+\boldsymbol{G}_s)\boldsymbol{\rho}], \tag{17}$$

$$-i\frac{d}{dz}\Psi_n(\boldsymbol{\rho},z)=\sum_{s=0}^{N_F-1} d_{sn}(z)\exp[i(\boldsymbol{k}_\parallel+\boldsymbol{G}_s)\boldsymbol{\rho}]. \tag{18}$$

At the matching plane we use the notation

$$f_{sn}\equiv f_{sn}(0),\quad d_{sn}\equiv d_{sn}(0).$$

We get rid of the mismatch in the values of $\Phi(\boldsymbol{\rho},0)$ by constructing continuous auxiliary functions $\chi_n(\boldsymbol{\rho},z)$, which are defined in the whole space:

$$\chi_n(\boldsymbol{\rho},z)=\begin{cases}\Psi_n(\boldsymbol{\rho},z), & z<0\\ \displaystyle\sum_{s=0}^{N_F-1} f_{sn}\phi_s(\boldsymbol{\rho},z), & z\geqslant 0.\end{cases} \tag{19}$$

The trial function

$$\tilde{\Phi}(\boldsymbol{\rho},z)=\sum_{n=0}^{N_{sol}} b_n\chi_n(\boldsymbol{\rho},z) \tag{20}$$

is constructed so as to yield correct asymptotic behavior, e.g., $b_0=1$, $a_0^-=0$ for electrons incident from the solid [Eqs. (11) and (12)] and $b_0=0$, $a_0^-=1$ for LEED states [Eqs. (15) and (16)]. The trial function is continuous, but each Fourier component has a mismatch in derivative:

$$m_s=\sum_{n=0}^{N_{sol}} b_n\Delta d_{sn},\quad s=0,\dots,N_F-1,$$

$$\Delta d_{sn}=(d_{sn}-f_{sn}k_s). \tag{21}$$

In the simple matching[2] the coefficients b_n are determined by equating m_s to zero, i.e., by an exact matching of N_F Fourier components. In that case it is necessary to include $N_{sol}=N_F$ solutions and the rest of the Fourier components are left unmatched. Experience shows that the cases are frequent in which the residual mismatch is not physically acceptable and the situation cannot be improved by increasing N_{sol}.

An alternative method to construct the solution for the semi-infinite crystal has been proposed by Bross,[13] who applied a bivariational method to obtain the wave function as a solution that yields a stationary value of the transmission coefficient. For the trial function (20) this approach leads to equation

$$\delta\theta=0,\quad \theta=\sum_s f_s^* m_s, \tag{22}$$

$$f_s=\sum_n b_n f_{sn}. \tag{23}$$

The physical meaning of Eq. (22) is transparent: Re(θ) is the current nonconservation at the surface and for a smooth function θ vanishes. An important advantage of this procedure over the simple matching is that N_{sol} is now independent of N_F. The mismatch is allowed to distribute over all the N_F Fourier components and the freedom can be used to diminish the integral slope mismatch against the simple matching. However, Bross's method has a shortcoming. θ is not a positive-definite quantity; consequently, the mismatches due to different $\boldsymbol{G}_s$ may compensate each other, thus providing a good current conservation, but producing a solution that is far from smooth.

To construct Φ Appelbaum and Hamann[4] used a least-squares method, i.e., minimized the quantity

$$M=\sum_s |m_s|^2=\sum_{n,n'} b_n b_{n'}^*\sum_s \Delta d_{sn}\Delta d_{sn'}^*, \tag{24}$$

by solving the equation $\delta M=0$. A disadvantage of this procedure is that all the Fourier components are treated equally and no preference is given to the $\boldsymbol{G}_s$ according to their individual contributions to the solution Φ. The mismatch is uniformly distributed over the vector set and large $\boldsymbol{G}_s$, for which the amplitudes f_{sn} are very small, can contribute to the mismatch considerably. Being the output of the variational procedure (8), which does not yield exact wave functions, the small Fourier coefficients $f_{sn}(z)$ in Eq. (17) are not reliable. Therefore, matching the corresponding Fourier components has no physical meaning.

B. Self-consistent matching scheme

A simple way to damp the unphysical contributions is to multiply each $|m_s|^2$ in Eq. (24) by the weight W_s with which the component enters the solution:

$$W_s = |f_s|^2 = \left| \sum_n b_n f_{sn} \right|^2. \tag{25}$$

In turn, the coefficients b_n are the solution of the variational equation

$$\delta\mu = 0,$$

$$\mu = \sum_s W_s |m_s|^2 = \sum_{n,n'} b_n b^*_{n'} B_{n'n},$$

$$B_{n'n} = \sum_s W_s \Delta d_{sn} \Delta d^*_{sn'}, \tag{26}$$

so that the Eqs. (25) and (26) must be solved self-consistently. Of course, any (increasing) function of W_s can be used to give preference to physically significant contributions and the mere weights seem to be the simplest and the most natural choice.

In the case that Φ is a propagating solution we minimize the weighted derivative mismatch μ under the constraint $b_0 = 1$ $(0 \leqslant n,n' \leqslant N_{sol})$. At the ith iteration step we minimize the quantity

$$\mu^i = \sum_s W_s^{i-1} |m_s|^2 \tag{27}$$

by solving a system of linear equations for b_n:

$$\hat{B}\boldsymbol{b} = \boldsymbol{\beta}, \quad \beta_n = B_{n0}. \tag{28}$$

In the case that Φ is a surface state $(1 \leqslant n,n' \leqslant N_{sol})$ we minimize μ^i under the integral constraint

$$\sum_s |f_s|^2 = 1, \tag{29}$$

which leads to a generalized symmetric eigenvalue problem

$$\hat{B}\boldsymbol{b} = \mu \hat{A}\boldsymbol{b}, \quad A_{n'n} = \sum_s f_{sn} f^*_{sn'}. \tag{30}$$

The solution we seek corresponds to the lowest eigenvalue.

To start with we use the scheme of Appelbaum and Hamann, i.e., at the first iteration we choose $W_s^0 = 1$ for all s. We assume the procedure to converge when

$$\frac{\Sigma_s |W_s^i - W_s^{i-1}|}{\Sigma_s W_s^i} < \alpha,$$

α being about 0.01. For propagating solutions the procedure converges rapidly $(i < 10)$. When E falls in a bulk energy gap the convergence slows down with the distance of E from the surface state energy E_s. The self-consistent procedure is easily transferred to the case of LEED states, where the asymptotic condition (15) implies the following constraint on b_n:

$$\sum_{n=1}^{N_{sol}} |b_n f_{0n}|^2 = |1 + a_0^+|^2. \tag{31}$$

C. Comparison of the matching schemes

We now compare the three variational matching schemes, namely, the bivariational approach of Bross,[13] the derivative-only-based method of Appelbaum and Hamann,[4] and the above nonlinear scheme. We consider two criteria of the quality of solution. The first is an upper estimate of the current mismatch caused by the residual discontinuity in slope at the surface,

$$\Delta F = \sqrt{\sum_s \{\mathrm{Re}[f_s^* m_s]\}^2}, \tag{32}$$

and the second is a mean square derivative mismatch, which is the actual measure of smoothness of the wave function at the surface

$$\Delta M = \sqrt{\frac{\Sigma_s |f_s^* m_s|^2}{\Sigma_s |f_s|^2}}. \tag{33}$$

As an example we consider normal-incidence LEED states for the (100) surface of fcc aluminum. The vacuum level was taken at $V_0 = 0.93$ Ry above the muffin-tin zero, which corresponds to a work function of 4.41 eV.[14] The plane $z = 0$ was located at half the interlayer spacing from the (100) atomic plane.

Figure 2 shows the energy dependence of the values ΔF and ΔM, which characterize the quality of the LEED states constructed from the same functions χ_n [see Eq. (19)] by the three schemes. The curves in the upper panel show that the self-consistent scheme yields the smoothest solution for all energies. Depending on the energy, one of the other curves closely approaches the self-consistent result, and over the whole energy region the three methods yield errors of the same order of magnitude. However, the curves in the lower panel suggest that the solutions may be unstable to these errors: In the interval 24–25 eV the method of Appelbaum and Hamann leads to the flux mismatch an order of magnitude larger than in the other two methods; apparently it finds a totally different solution.

Nevertheless, except for a number of intervals, over a wide energy region from 10 to 40 eV the three schemes yield physically similar results and the character of the resulting LEED states is stable to the residual mismatch at the surface. In practical calculations we rely upon the self-consistent matching scheme because at any energy its output is con-

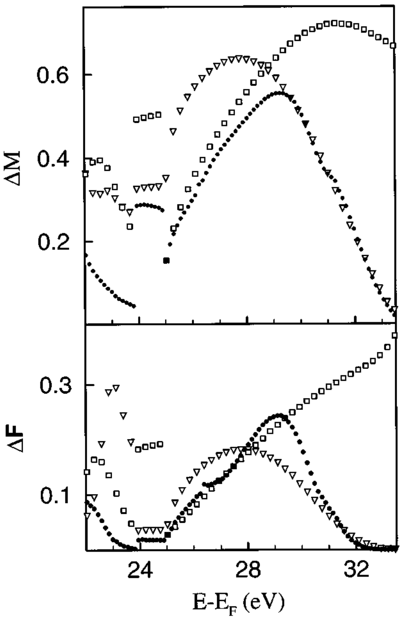

FIG. 2. Energy dependence of the matching error (upper panel) and of the current nonconservation due to the mismatch (lower panel) by three matching schemes: the bivariational method (22), triangles; the derivative-only approach (24), squares; and the nonlinear scheme, (26) and (27), dots.

firmed either by the result of the bivariational procedure or by that of the pure-derivative approach.

D. Conductance index

The above investigation makes it clear that constructing the LEED states within the complex band-structure approach is a time-consuming procedure (it involves diagonalization of the matrix of twice the dimension of the Hamiltonian matrix), which may fail to yield a reliable output. Thus it is desirable to have a guide that would in advance indicate the unsafe regions of the energy spectrum and point out the critical points of the band structure.

The critical points by themselves are studied experimentally by very-low-energy electron diffraction[15] (VLEED) and by target current spectroscopy (TCS),[16] so we shall construct a function that simulates the current carried by the LEED state.

The time-saving approach presently used to relate the $\boldsymbol{k}_{\parallel}$-projected real band structure to VLEED or TCS data is the conducting-Fourier-component[17] (CFC) approximation, where one relies upon the similarity between the function $f_{0n}(z)$ [defined by Eq. (17)] and a plane wave. In contrast to the CFC approximation, the approach to be introduced in this section explicitly takes into account the matching conditions at the surface.

We start with an approximation of a single transmitted Bloch wave $\Psi_m(\boldsymbol{\rho},z)$, i.e., we assume that in Eq. (16) $b_n \propto \delta_{nm}$. Then we match the incident wave ϕ_0^- and the main reflected wave ϕ_0^+ to the zeroth Fourier component both in value f_{0m} and in slope d_{0m} [see Eqs. (17) and (18)] to get the two coefficients b_m and a_{0m}^+, the other reflected plane waves being matched only in value [see Eq. (19)]. Thereby we obtain the current in the vacuum

$$T_m^v = 1 - \frac{1}{k_0} \sum_s |a_{sm}^+|^2 \, \mathrm{Re}(k_s). \tag{34}$$

The LEED state is normalized so that the current carried by the incident electron is unity. T_m^v is the transmitted current insofar as the above assumption is valid. A simple way to assess the validity of the single Bloch wave approximation is to evaluate the current nonconservation by comparing T_m^v to the current in the bulk T_m^b, which is calculated as an integral over the unit cell

$$T_m^b(E,\boldsymbol{k}_{\parallel}) = \frac{|b_m|^2}{k_0 \Omega} \left\langle \Psi_m \middle| -i\frac{d}{dz} \middle| \Psi_m \right\rangle. \tag{35}$$

Evanescent waves are excluded from this consideration because they carry zero current.

Thereby the validity can be expressed by a quantity ξ_m defined as

$$\xi_m = \begin{cases} |T_m^v/T_m^b|^\gamma, & |T_m^v| \leq |T_m^b| \\ |T_m^b/T_m^v|^\gamma, & |T_m^v| > |T_m^b|, \end{cases} \tag{36}$$

where ξ_m is less than unity unless there is a perfect current conservation. γ is an arbitrary positive scaling factor; in this work we have chosen $\gamma = 1$. We calculate the product

$$K_m = T_m^v \xi_m$$

and take the largest K_m for a given energy as a *conductance index* for this energy.

The conductance index is expected to point out the critical points of the real band structure because both multipliers react on a change in matching conditions and one of them ξ_m reflects changes in slope of the band:

$$\frac{dE_{\boldsymbol{k}m}}{dk_\perp} = \frac{\hbar}{m} \left\langle \Psi_m \middle| -i\frac{d}{dz} \middle| \Psi_m \right\rangle. \tag{37}$$

In the present calculations we have observed only the case $0 < T_m^v/T_m^b < 1$ and the single-carrier approximation has turned out to be valid over the energy regions from 10 to 18 eV and from 30 to 60 eV. An interesting situation is encountered in the energy region from 25 to 30 eV. There a single-constituent wave function yields a good current conservation (and for this reason this is just the solution chosen by the bivariational procedure); however, the wave function is far from smooth. The self-consistent method is only able to diminish the mismatch slightly and the current nonconservation of the LEED state becomes rather large. We infer that in this region the exact solution contains steeply decaying waves, which are not included in the present calculation.

The matching instabilities occur in the energy intervals where the conductance index is close to zero. In such cases the incident beam couples to an evanescent wave and either reflects (as predicted by the conductance index) or, via matching, transfers the current to the propagating Bloch states. In both cases the requirements to accuracy of the Fourier components are rather stringent because more than one surface coordination sphere is involved. In addition, the evanescent waves, which now strongly contribute to the wave function, may have large $\mathrm{Im}(k_\perp)$ and, consequently, a poor accuracy.

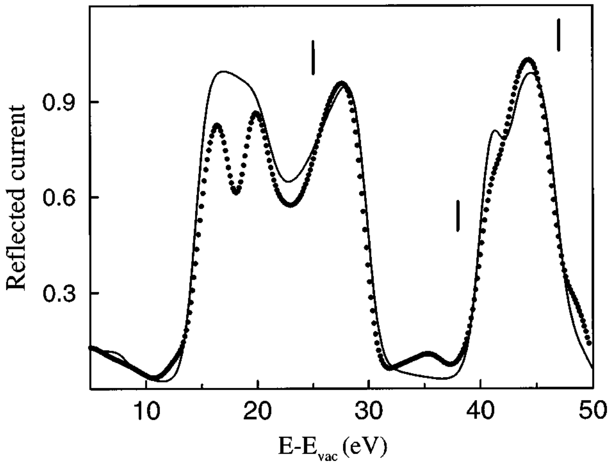

FIG. 3. LEED spectrum for the (100) surface of Al. *Ab initio* calculation (dots) and the single-carrier approximation $1-K(E)$; see Sec. III D. The curves are convoluted with a Gaussian of 2 eV full width at half maximum. Vertical bars show the energy location of the experimentally observed maxima (Ref. 18).

E. Comparison with LEED measurements

Figure 3 shows the theoretical normal incidence LEED spectrum for an energy region 5–50 eV above the vacuum level. We show the intensity integrated over all the beams. Our calculations are in a good agreement with the measurements by Jona[18] (incidence angles were $\theta=6°$, $\varphi=45°$), who observed a strong specular reflection between 20 and 30 eV with a maximum at ~25 eV and a broad maximum centered at ~47 eV.

Our calculations predict a strong reflection in the interval 15–30 eV and a higher energy peak at 44 eV. A weak structure due to the $\overline{11}$ beam is experimentally observed at ~38 eV; in the theoretical curve the corresponding maximum is located at ~35 eV. The energy location of experimental features is marked by vertical bars in Fig. 3.

The most pronounced disagreement with the experiment is observed below 20 eV, where our calculations predict a negligible absorption. In this interval ($19<E-E_F<24.5$ eV) the incident beam couples strongly with the evanescent waves that decay slowly into the solid; see Fig. 4. Hence the incident electron penetrates deeply into the solid, thus having a high probability to be absorbed as a result of inelastic processes. Such processes were not taken into account in the present calculation, which explains the observed disagreement. The higher-energy features at 38 eV and 44 eV in the calculated curves are shifted by ~3 eV to lower energies, which can be ascribed to inadequacy of the local-density approximation (LDA)–based one-electron approach we have used.

IV. CALCULATION OF THE SURFACE STATES

We now apply the inverse ELAPW $\mathbf{k}\cdot\mathbf{p}$ method and the variational matching scheme to calculate the surface state in the local band gap in the valence-band energy spectrum of aluminum along the Γ-X direction, $\boldsymbol{k}=(0,0,k_\perp)$ (see Ref. 21). The bottom of the gap is at the point X_4' $(-2.81$ eV) and the top is at X_1 $(-1.83$ eV).

The eigenvalue procedure (9) now generates only evanescent states and we match their linear combination at the surface to a linear combination of the evanescent plane waves (13), $\mathrm{Im}k_s>0$. Within the formalism of simple matching the surface state energy is calculated as the energy at which the determinant of the matching matrix vanishes.[20] Similarly, in the variational matching we expect the surface state to appear at the energy where a smooth solution can be constructed. As a measure of smoothness we use the weighted average mismatch

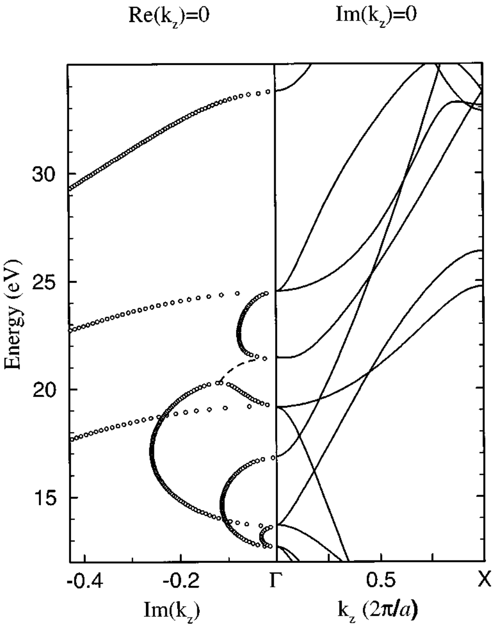

FIG. 4. The left panel shows real lines of the complex band structure of Al in the [100] direction calculated by the inverse ELAPW $\mathbf{k}\cdot\mathbf{p}$ method (circles). The right panel shows the real band structure in the Γ-X direction (solid lines). $\boldsymbol{k}$ vectors are measured in units of $2\pi/a$. Our results are in a good agreement with calculations of Wachutka (Ref. 19).

$$Q=\sum_s |f_s^* m_s|. \tag{38}$$

The non-self-consistent result for Q $[\delta M=0$; see Eq. (24)] changes rapidly and shows a sharp minimum at $E_s=-2.37$ eV. The self-consistent solution $[\delta\mu=0$; see Eq. (26)] at this energy is identical to the non-self-consistent one (the convergence is achieved at the second iteration), but over a narrow interval around E_s the self-consistent solution is much smoother. It appears that the self-consistent method succeeds in constructing an approximate solution in the vicinity of the surface state energy. The result of the simple matching is in agreement with that of the variational approach; the determinant of the matching matrix vanishes at $E=-2.30$ eV.

The surface state energy has turned out to be rather sensitive to the height of the steplike surface barrier. With increasing the vacuum level from E_F to $V_0=5$ Ry the energy E_s moves steadily from almost the bottom of the gap to higher energies with the saturation point at ~-1.9 eV. However, it is important that with any choice of $V_0>E_F$ the surface state is observed. Thus we expect the simple steplike simulation of the surface barrier to yield at least qualitatively

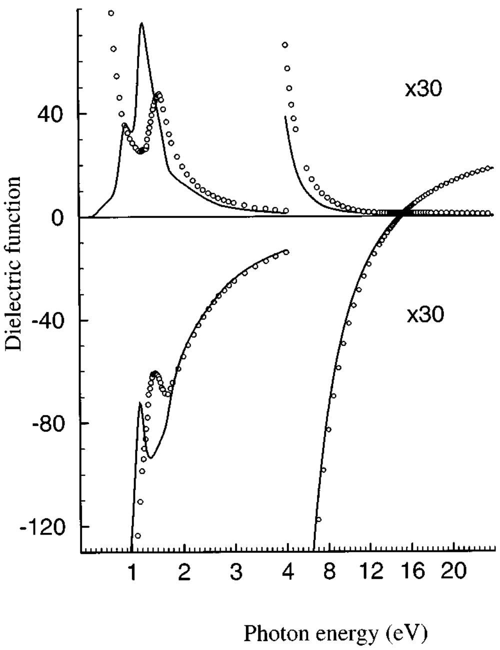

FIG. 5. Imaginary (upper panel) and real (lower panel) parts of the DF of Al metal. *Ab initio* spectra are shown by solid lines. Experimental results (Ref. 23) are shown by open circles.

reliable results. Nevertheless, a corrugated potential can be treated in an analogous way, whereas a reconstructed surface needs additional matching planes. Because of the knowledge of the whole wave function the potential can be iteratively brought to self-consistency.

V. ERRORS DUE TO THE ONE-ELECTRON APPROXIMATION

The experimental band-gap parameters derived in Ref. 21 from the photoemission measurements were $E(X_4')=-2.83$ eV and $E(X_1)=-1.15$ eV and the surface state was experimentally observed at -2.75 eV. Several band-structure calculations have been reviewed in Ref. 21 and it has been concluded that none of them reproduces correctly the experimentally observed energy location of the X_1 state. Our results are closest to the APW calculation[22] $E(X_4')=-2.76$ eV and $E(X_1)=-1.77$ eV. Although it has been supposed in Ref. 21 that the discrepancy may be due to experimental problems, namely, to a possible $\boldsymbol{k}$ smearing, it does not seem that LDA-based calculations are able to describe precisely the spectral properties of aluminum because discrepancies of the same order of magnitude are observed in the optical properties of Al (see Fig. 5) and in the valence-band width.[21]

To assess the validity of the one-electron approximation adopted in the present work we compare in Fig. 5 our calculated dielectric function (DF) of aluminum with the measurements of Ref. 23. The low-energy structures are seen to be shifted to low energy by 0.3 eV from their measured locations, so one should not expect a better agreement with photoemission measurements.

On the other hand, the intraband contribution to the real part of the DF is perfectly reproduced within the one-electron approach. It has a Drude-like form[24]

$$\varepsilon_1^{intra}=1-\frac{\omega_p^2}{\omega^2}, \tag{39}$$

with the plasma frequency $\omega_p=14.85$ eV calculated as an integral over the Fermi surface. Above $\hbar\omega=2$ eV the intraband contribution to ε_1 dominates and the agreement with the measured spectrum is excellent. The experimental value for the plasma frequency is 15.05 eV.

VI. CALCULATION OF THE PHOTOEMISSION SPECTRA

In the one-step model of photoemission[25] the photocurrent is determined by dipole transitions from the initial states Ψ_i to the time-reversed LEED state Φ^*_{LEED},

$$I(E)\propto\sum_i |\langle\Phi^*_{\text{LEED}}(E,\boldsymbol{k}_\parallel)|(\boldsymbol{A}\cdot\hat{\boldsymbol{P}}+\hat{\boldsymbol{P}}\cdot\boldsymbol{A})|\Psi_i\rangle|^2$$

$$\times\delta(E-E_i-\hbar\omega). \tag{40}$$

The LEED states were calculated as explained in Sec. III and the initial states were obtained by the direct ELAPW $\mathbf{k}\cdot\mathbf{p}$ method. In principle, the $\mathbf{k}\cdot\mathbf{p}$ formalism is not crucial for calculating the initial states; however, using the $\mathbf{k}\cdot\mathbf{p}$ method considerably accelerates evaluation of the $\boldsymbol{k}$-nonconserving momentum matrix elements (MME's). In computing the ''oblique'' MME's the plane-wave representation for Φ_{LEED} and Ψ_i is the most convenient. In the $\mathbf{k}\cdot\mathbf{p}$ method the transfer matrix between the APW's and the plane waves is computed only once, whereas in a non-$\mathbf{k}\cdot\mathbf{p}$ method this time-consuming procedure must be repeated for each $\boldsymbol{k}$ point.

Electron absorption is introduced at the last stage of the calculation as the optical potential V_i, an imaginary part of the potential in the solid. The effect of the optical potential is taken into account within the approximation so that it does not affect the periodic part of the Bloch constituents of the LEED state [see Eq. (16)]. Thus in the APW decomposition of the wave function Ψ_n [see Eq. (7)] the coefficients $\boldsymbol{C}_{in}$ are left unchanged, but the z component of the Bloch vector changes to become complex for the propagating solutions of Eq. (8),

$$k_\perp'=k_\perp+\kappa_1+i\kappa_2. \tag{41}$$

With the imaginary contribution iV_i to the Hamiltonian $\hat{H}$ Eq. (8) gives

$$\kappa_1=-\frac{1}{2}\left(V_z+\frac{V_i}{\kappa_2}\right), \tag{42}$$

$$\kappa_2=-\sqrt{\frac{\sqrt{V_z^4+16V_i^2}-V_z^2}{8}}, \tag{43}$$

$V_z>0$ being the velocity of the time-reversed constituent, which is calculated as an integral over the unit cell [see Eq. (37)]. For an evanescent state the velocity is zero and the Bloch vector $k_\perp=k_{\perp 1}+ik_{\perp 2}$ changes as

$$k_{\perp 1}'=k_{\perp 1}-\frac{V_i}{2k_{\perp 2}'}, \tag{44}$$

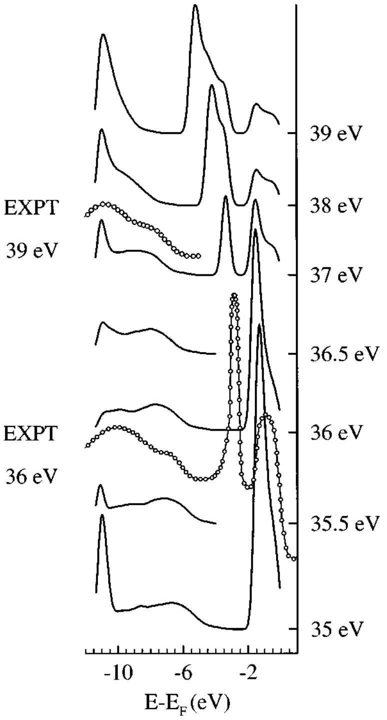

FIG. 6. Normal-emission photoelectron spectra for the Al (100) surface. Theory (solid lines) and the experiment (circles) are reproduced from Ref. 21. The theoretical spectra are convoluted with a Gaussian of 0.5 eV full width at half maximum. The origin of the intensity scale for each spectrum is marked by the photon energy.

$$k'_{\perp 2} = -\sqrt{\frac{\sqrt{k_{\perp 2}^4 + V_i^2} + k_{\perp 2}^2}{2}}. \tag{45}$$

The energy dependence of the optical potential was simulated by a Fermi-like step function

$$V_i(E) = \frac{V_i^{\infty}}{1+\exp[-(E-\omega_p)/R]}, \tag{46}$$

where $V_i^{\infty} = 3$ eV, $\omega_p = 15$ eV (see Sec. V), and $R = 10$ eV.

Figure 6 shows calculated photoelectron spectra for the photon energies from 35 to 40 eV. Emission from the surface state was not taken into account in this calculation. We compare the theoretical results with the measurements by Levinson, Greuter, and Plummer.[21] In this range two peaks due to direct transitions have been experimentally observed at low initial energies. No structures below the surface state energy were experimentally observed at $\hbar\omega = 30$ eV. In the experiment with increasing the photon energy from 36 to 39 eV the shoulder at $E_i \approx -7$ eV moves to lower energies and disappears at $\hbar\omega = 40$ eV. In our calculations the corresponding structure becomes visible at $\hbar\omega = 32$ eV; at this frequency it is located at $E_i = -3.5$ eV, so that it cannot be visible in the experiment because of the strong broad peak due to the surface state at $E_i = -2.75$ eV. We observe this structure moving from -6.5 to -8 eV with the photon energy increasing from 35 to 37 eV. In other words the calculated final states are shifted by ~ 2 eV to lower energies.

The lowermost structure (at ~ -11 eV) is due to the initial states at the point Γ (the bottom of the valence band). At $\hbar\omega = 32$–35 eV (not shown here) it originates from a band-gap emission (see Fig. 6), i.e., the intensity is determined by transitions to the evanescent constituents of the time-reversed LEED state. Above $\hbar\omega = 35.5$ eV we observe direct transitions in the vicinity of the point Γ; hence, for the photon energies 35–36 eV the final states are far from free-electron-like. The negligible dispersion of the lowermost structure is explained by the steepness of the final-state band. The propagating constituents are strongly damped by the optical potential and therefore the transitions occur in the vicinity of the crystal surface. As a result, the shape and the intensity of the lowermost peak strongly depend upon the form of the surface potential barrier as well as upon the way of treating the electron absorption. In the present calculation both effects were included in the simplest manner; nevertheless, our results agree qualitatively with the measurements of Ref. 21, wherein going from $\hbar\omega = 36$ eV to $\hbar\omega = 39$ eV the lowermost structure shifts to lower energies by ~ 0.5 eV and its intensity grows.

Above $\hbar\omega = 40$ eV this peak disappears because of the wide gap at the Γ point between $E - E_F = 25$ eV and 33 eV. In our calculations the structure below -10 eV is observed again for photon energies between 44 and 52 eV. From $\hbar\omega = 42$ to 48 eV we see a single maximum that moves from -8 eV at $\hbar\omega = 42$ eV to -11 eV at $\hbar\omega = 46$ eV. It remains at -11 eV up to $\hbar\omega = 48$ eV and at higher frequencies it splits into two peaks. In the experiment in the frequency region from 45 to 52 eV a single maximum was observed; its energy location changed irregularly with frequency between -9.5 and -10.6 eV.[21]

Considering that the finite lifetime of the hole, not included in the present calculation, smears out the frequency dependence of the structures and affects their shape, the present calculation unambiguously determines the origin of the peaks and correctly predicts their dispersion. A comparison with the experiment infers that for the energies between 20 and 30 eV above the Fermi level the real part of the self-energy is about 2 eV and it increases with energy to at least 3 eV at 40 eV (see Sec. III E).

VII. CONCLUSION

We have extended the Bloch wave method for surfaces to the case of a realistic singular crystal potential. A milestone of the computational procedure is the extended radial basis set, which makes the $\mathbf{k}\cdot\mathbf{p}$ formulation of the band-structure problem practically applicable. Within the $\mathbf{k}\cdot\mathbf{p}$ method the inverse band-structure problem is solved by means of linear algebra, which leads to an efficient pseudopotential-like procedure.

The computing time required to calculate the photoemission spectra for a given $\boldsymbol{k}_{\parallel}$ is not longer than for a self-consistent band-structure calculation and the limitations of the method are exactly the same as in the modern band-structure methods. We expect the method to be promising in many applications of surface science.

We have applied the present method to aluminum and have found reasonable agreement with the LEED and photoemission measurements. Some of the features of the photoelectron spectra of Al are directly related to the real band structure, which is far from free-electron-like up to 50 eV above the Fermi level; however, the whole picture can only be understood in terms of the complex band structure.

In the present work we have constructed the electron wave functions by matching the solutions of the two half spaces at the interface. This approach seems to be not devoid of shortcomings. Though the matching scheme used in this work performs considerably better than the other presently used schemes, the current nonconservation due to the residual mismatch is still not negligible. By employing the matching one concentrates the error at the matching plane, but it may be an improvement to smear the error over a z interval in the surface region. This may be implemented by constructing a smooth trial function in order that the wave function Φ be obtained by solving the Schrödinger equation in the surface region by a variational method.

ACKNOWLEDGMENTS

The authors are grateful to F. Starrost for useful comments and helpful suggestions and to Dr. O. V. Krasovska for programming assistance. E.E.K. gratefully acknowledges the support by a grant of the Deutsche Forschungsgemeinschaft.

---

*Permanent address: Institute of Metal Physics, National Academy of Sciences of Ukraine, Vernadskogo 36, 252680, Kiev-142, Ukraine.

[1] P. M. Marcus and D. W. Jepsen, Phys. Rev. Lett. **20**, 925 (1968).

[2] J. B. Pendry, J. Phys. C **2**, 2273 (1969).

[3] J. B. Pendry, Surf. Sci. **57**, 679 (1976).

[4] J. A. Appelbaum and D. R. Hamann, Phys. Rev. B **6**, 2166 (1972).

[5] J. B. Pendry, *Low Energy Electron Diffraction* (Academic, London, 1974).

[6] M. Grass, J. Braun, and G. Borstel, Phys. Rev. B **47**, 15 487 (1993).

[7] E. E. Krasovskii, preceding paper, Phys. Rev. B **56**, 12 866 (1997).

[8] E. E. Krasovskii and W. Schattke, Solid State Commun. **9**, 775 (1995).

[9] E. Wimmer, H. Krakauer, M. Weinert, and A. J. Freeman, Phys. Rev. B **24**, 864 (1981).

[10] O. K. Andersen, Phys. Rev. B **12**, 3060 (1975).

[11] In practice we use a pure APW representation of the extended set (see Ref. 8), so that all the basis functions in Eq. (3) are $\boldsymbol{k}_0$-dependent Bloch waves.

[12] F. Aryasetiawan and O. Gunnarsson, Phys. Rev. B **49**, 7219 (1994).

[13] H. Bross, J. Phys. F **12**, 2883 (1982).

[14] J. G. Grepstad, P. O. Gartland, and B. J. Slagsvold, Surf. Sci. **57**, 348 (1976).

[15] V. N. Strocov, Int. J. Mod. Phys. B **9**, 1755 (1995).

[16] J. V. Peetz, W. Schattke, H. Carstensen, R. Manzke, and M. Skibowski, Phys. Rev. B **46**, 10 127 (1992).

[17] V. N. Strocov, Solid State Commun. **78**, 845 (1991); V. N. Strocov and S. A. Komolov, Phys. Status Solidi B **167**, 605 (1991).

[18] F. P. Jona, IBM J. Res. Dev. **14**, 444 (1970).

[19] G. Wachutka, Phys. Rev. B **34**, 8512 (1986).

[20] F. Forstmann, Z. Phys. **235**, 69 (1970).

[21] H. J. Levinson, F. Greuter, and E. W. Plummer, Phys. Rev. B **27**, 727 (1983).

[22] F. Szmulowicz and B. Segal, Phys. Rev. B **21**, 5628 (1980).

[23] J. H. Weaver, C. Krafka, D. W. Lynch, and E. E. Koch (unpublished).

[24] H. Ehrenreich and M. A. Cohen, Phys. Rev. **115**, 789 (1951).

[25] P. J. Feibelman and D. E. Eastman, Phys. Rev. B **10**, 4932 (1974).